Catalysis Today 157 (2010) 160–165

Contents lists available at ScienceDirect

Catalysis Today

journal homepage: www.elsevier.com/locate/cattod

Modified cryptomelane-type manganese dioxide nanomaterials for preferential oxidation of CO in the presence of hydrogen

W.Y. Hernández[a,*], M.A. Centeno[a], F. Romero-Sarria[a], S. Ivanova[a], M. Montes[b], J.A. Odriozola[a]

[a] Departamento de Química Inorgánica e Instituto de Ciencia de Materiales de Sevilla, Centro Mixto Universidad de Sevilla-CSIC, Avda. Américo Vespuccio 49, 41092 Seville, Spain
[b] Grupo de Ingeniería Química, Dpto. Química Aplicada, Fac. Ciencias Químicas de San Sebastián, Paseo Manuel Lardizábal 3, 20018 San Sebastián, Spain

ARTICLE INFO

Article history:
Available online 14 April 2010

Keywords:
Octahedral molecular sieve (OMS)
Preferential oxidation of CO (PROX)
Manganese dioxide
Cryptomelane
Transition metal-modified MnO_2

ABSTRACT

Transition metal (Cu, Co, Ni and Zn)-modified cryptomelane-type manganese dioxide nanomaterials were synthesized by the milling method. The obtained solids have been characterized by means of X-ray diffraction (XRD), scanning electron microscopy and transmission electron microscopy (SEM and TEM), N_2 adsorption–desorption measurements at 77 K, Raman spectroscopy and temperature programmed reduction (TPR-H_2) showing similar structural and textural properties. All the solids were active in the preferential oxidation of CO in the presence of hydrogen (PROX), being the modified with copper the most active. The catalytic activity correlates fairly well with the TPR results, finding higher CO conversion for the material with higher reducibility (OMS-Cu). The O_2 selectivity, measured as $([CO]_{in} - [CO]_{out}/2[O_2]_{in} - [O_2]_{out}) \times 100$, is very similar for all synthesized materials.

1. Introduction

The presence of minute amounts of CO in hydrogen flows poisons fuel cell electrodes [1,2]. This has greatly contributed to the last years enormous interest in the preparation of active and selective catalysts for CO oxidation in the presence of large amounts of H_2 in the gas feed, where the main reactions occurring are:

$$CO + ½O_2 \rightarrow CO_2, \quad \Delta H^\circ = -283\,\mathrm{KJ\,mol^{-1}} \quad (1)$$

$$H_2 + ½O_2 \rightarrow H_2O, \quad \Delta H^\circ = -242\,\mathrm{KJ\,mol^{-1}} \quad (2)$$

Manganese-based catalysts, especially in Hopcalite-like compounds [3,4], have been reported as active and selective in many oxidation reactions. In addition to this, studies devoted to elucidate the catalytic effects of various crystallographic phases of Mn in oxidation reactions have been reported [5–9]. Cryptomelane, an octahedral molecular sieve, is an allotropic form of manganese oxide having a well-defined 2×2 tunnel structure (OMS-2) consisting a double chains of edge-shared MnO_6 octahedra and corner-sharing of the double chains (general formula $K_xMn_8O_{16}$). The pore size of the tunnel is 0.46 nm [10]. The average manganese oxidation state in cryptomelane is around 3.8 resulting from the presence of mainly Mn^{4+} and only small amounts of Mn^{3+} and Mn^{2+}. Potassium aquacomplex ions are situated inside the tunnels to provide charge balance and to stabilize the structure. Due to its porous structure and mixed valence of manganese species, cryptomelanes have been extensively explored for potential applications such as molecular sieves, catalysts and rechargeable battery materials [11–13]. In particular, they have shown excellent catalytic activities towards oxidation reactions [6,7]. In this sense, it has been reported that the incorporation of Cu, Co and Ni into the channels or in the structure of OMS-2 materials promotes the generation of defects and enhances the lattice oxygen mobility [14], improving their catalytic performances in the CO oxidation.

The present study focuses on the preparation, characterization and evaluation of the catalytic activity in the preferential CO oxidation (in presence of hydrogen), of cryptomelane-type manganese dioxide nanomaterials, prepared by the milling method [15] and modified with different transition metal cations (Cu, Co, Ni, and Zn) in order to modify its electronic and catalytic properties.

2. Experimental

2.1. Synthesis

Cryptomelane solids were prepared by solid-state reaction between Mn^{7+} and Mn^{2+} species in a high-energy ball milling with stainless steel balls (12 balls, 20 mm diameter) and jar [7,15]. The relationship ball-weight/solid-weight was 10/1. In a typical experiment, $KMnO_4$ (Panreac 99.0%) and $Mn(CH_3COO)_2{\cdot}4H_2O$ (Panreac 99.0%) (stoichiometric ratio 2:3) were mixed homogeneously and then milled for 1 h at 300 rpm. The resulting black solid was kept 4 h in a capped bottle at 80 °C. The obtained product was thoroughly

* Corresponding author at: Instituto de Ciencia de Materiales de Sevilla, Universidad de Sevilla-CSIC, Spain. Tel.: +34 954489501x9221; fax: +34 954460665.
E-mail address: willinton.yesid@icmse.csic.es (W.Y. Hernández).

0920-5861/$ – see front matter © 2010 Elsevier B.V. All rights reserved.
doi:10.1016/j.cattod.2010.03.010

washed with water until neutrality, dried at 80 °C overnight and finally calcined at 450 °C for 2 h.

Metal-modified cryptomelanes were prepared by adding the corresponding metal acetate (Cu, Co, Ni, or Zn) to the $KMnO_4$ and $Mn(CH_3COO)_2{\cdot}4H_2O$ mix during the milling, employing metal/(Metal + Mn^{2+}) molar ratio of 0.1.

The series of synthesized materials were named OMS-X, where X corresponds to the transition metal used as dopant.

2.2. Characterization

The chemical composition of the samples was determined by X-ray fluorescence spectrometry (XRF) in a Panalytical AXIOS PW4400 sequential spectrophotometer with a rhodium tube as the source of radiation.

X-ray diffraction (XRD) analyses were performed on a Siemens D 500 diffractometer. Diffraction patterns were recorded with Cu Kα radiation (40 mA, 40 kV) over a 2θ-range of 10–80° using a position-sensitive detector with a step size of 0.01° and a step time of 7 s. The reflection from the (2 1 1) plane was used for the determination of the average crystallite size, D, calculated from the Scherrer equation.

BET specific surface areas were measured through nitrogen adsorption–desorption isotherms at liquid nitrogen temperature in a Micromeritics ASAP 2000 apparatus. Before analysis, the samples were outgassed for 2 h at 150 °C in vacuum. The Barrett–Joyner–Halenda (BJH) method was used for determining the pore size distributions, in every case the desorption data were used.

A homemade apparatus was used for obtaining the TPR profiles. In the experiments 50 mg of sample were placed in the reactor and submitted to a gas mixture flow, constituted by Ar (50 mL/min) and H_2 (2 mL/min), then a heating rate of 15 °C/min to a final temperature of 900 °C was set. The H_2 consumption was monitored using a TCD detector.

The Raman spectra were recorded in a dispersive Horiva Jobin Yvon LabRam HR800 Microscope, with a 20 mW He–Ne green laser (532.14 nm) working at 0.2 mW power and with a 600 g mm^{-1} grating. The microscope used a 100× objective and a confocal pinhole of 500 μm. These conditions are necessary to prevent decomposition or denaturation of the samples by the incidence of the laser. The Raman spectrometer is calibrated using a silicon wafer.

2.3. Catalytic activity

Preferential oxidations of CO in the presence of hydrogen (PROX) reactions were carried out at atmospheric pressure in a stainless steel fixed bed reactor (9 mm inner diameter). A reaction mixture composed by 2% CO (Air Liquide, 99.997% pure, <3 ppm H_2O), 1% O_2 (Air Liquide, 99.999% pure, <3 ppm H_2O), 50% H_2 (Abelló Linde, 99.999% pure, ≤5 ppm H_2O) and N_2 (Abelló Linde, 99.999% pure, ≤5 ppm H_2O) as balance at 100 mL min^{-1} total flow. The automated, integrated micro-reactor system (®Microactivity Reference) employed for this reaction was designed by PID Eng & Tech Company.

The catalyst (100 mg, 100 < ϕ < 200 μm) was diluted in the adequate amount of crushed glass, having the same particle size, to obtain a bed height of 5 mm. Prior to all catalytic measurements, the samples were treated in a 21 vol.% O_2/N_2 mixture (30 mL/min) at 300 °C for 1 h. Products and reactants were separated and quantified by on-line gas chromatography (Agilent 7890A), provided with ®Haysep Q, ®Porapak Q and Mole-Sieve columns.

The CO conversion, O_2 conversion and O_2 selectivity were calculated according to Eqs. (3)–(5).

$$\text{CO conversion}\,(\%) = ([\text{CO}]_{\text{in}} - [\text{CO}]_{\text{out}}/[\text{CO}]_{\text{in}}) \times 100 \quad (3)$$

Table 1
Chemical composition and crystallite sizes (by XRD analysis), obtained for the synthesized materials.

Code	Atomic ratios (XRF)		Crystallite size, D (nm)
	K/M_T	M/M_T	
OMS	0.084	–	9.5
OMS-Cu	0.082	0.042	10.3
OMS-Co	0.083	0.023	10.4
OMS-Ni	0.078	0.010	9.5
OMS-Zn	0.082	0.008	10.8

M = Cu, Co, Ni or Zn, depending of the analyzed solid. M_T = Total metal: Mn + M + Fe (contamination).

$$\text{O}_2\text{ conversion}\,(\%) = ([\text{O}_2]_{\text{in}} - [\text{O}_2]_{\text{out}}/[\text{O}_2]_{\text{in}}) \times 100 \quad (4)$$

$$\text{O}_2\text{ selectivity}\,(\%) = ([\text{CO}]_{\text{in}} - [\text{CO}]_{\text{out}}/2[\text{O}_2]_{\text{in}} - [\text{O}_2]_{\text{out}}) \times 100 \quad (5)$$

3. Results and discussions

3.1. Chemical analysis, structure and morphology

The XRF results show the effective incorporation of the dopant cations in the synthesized materials, as seen in Table 1. The presence of iron, coming from the balls and jar used in the milling, is also detected. The K/MT ratio is very similar in all materials, indicating a similar charge, while the M/M_T ratio varies between 0.008 and 0.042, finding a higher uptake for Cu.

All the reflections in the XRD patterns, as shown in Fig. 1, clearly reveal that the as prepared materials only contain the cryptomelane-type crystalline phase (JCPDS 29-1020), namely, K-MnO_2 with an I-centered tetragonal structure (space group $I4/m$) [14]. No other phases are detected. The absence of CuO, NiO, CoO or ZnO diffraction lines might indicate that: (i) transition metal oxides are in low contents or have crystalline domains beyond the detection limit of XRD; (ii) transition metals are incorporated in the cryptomelane structure, with the formation of a solid solution; and/or (iii) transition metals are incorporated into the channels of cryptomelane structure, replacing K^+ ions. For the option (ii), the dopant cation would occupy only octahedral sites replacing Mn^{4+} or Mn^{3+} cations in MnO_6 octahedra from the parental structure. In the option (iii), the aqua complex of $M(H_2O)_n^{2+}$-type could be formed in the tunnels of cryptomelane. Taking into account the low quantity of water in our synthesis method (only coming from the water hydration of reactants and the acetate anions oxidation by $KMnO_4$) and the close relationship between the size of the tunnel and the radius of the aquacomplex, later can be discarded, therefore the

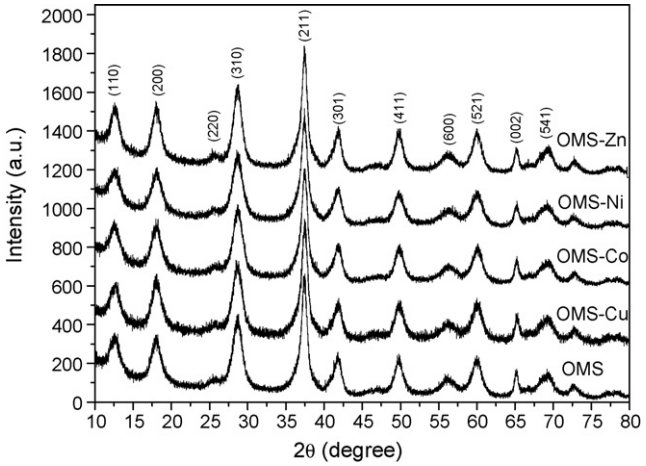

Fig. 1. XRD patterns of the synthesized materials.

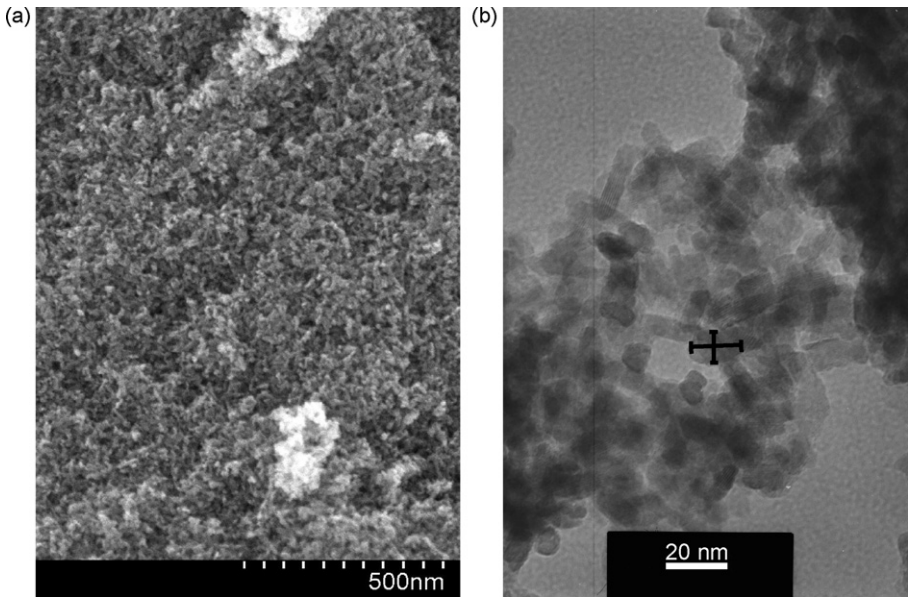

Fig. 2. Representative (a) SEM and (b) TEM images from OMS solid.

M^{2+} doping cation should only exist either in the framework of the material or as finely dispersed transition metal oxides supported on the cryptomelane phase.

The crystal domain size of the synthesized materials calculated from the XRD line broadening is shown in Table 1. The crystallite domain size, ca. 10 nm, is very similar for the all the synthesized materials and typical for the cryptomelane structures synthesized by the milling method [15]. From SEM and TEM observations (Fig. 2) and analysis of the XRD intensity ratio between (0 0 2) and (3 1 0) crystal planes (orthogonal planes), diffraction lines resulted in aspect ratios for the cryptomelane nanoparticles between 1 and 2 (nanorods), evidencing a low anisotropy in crystallite morphology, and suggesting that the growth along [0 0 1] is disfavored by the milling process [16]. Whatever the doping cation used in the synthesis, all the materials present the same nanoparticle morphology and aspect ratio, which is characteristic of the synthesis method employed.

3.2. Specific surface area and porosity measurements

The nitrogen adsorption–desorption isotherms for all the samples are similar. As an example, the isotherm obtained for the un-doped OMS solid is shown in Fig. 3. The isotherms indicate the presence of a mesoporous structure (IV type isotherm with H2 hysteresis loop) probably due to pores generated by the spaces between the nanoparticles [7,17]. All the catalysts present similar surface area, pore volume and average pore size diameter, a summary of the textural characteristics of all the materials is given in Table 2. The inset in Fig. 3 shows mesopore size distributions calculated by BJH method. The BJH plots show a relatively narrow pore size distribution in the range of 2.5–15 nm, indicating a uniform mesopore diameter of around 9 nm in close agreement with the calculated average pore size, Table 2.

Table 2
Textural properties of the synthesized materials.

Code	S_{BET} (m^2/g)	V_P (cm^3/g)	Pore size (nm)
OMS	124	0.34	7.8
OMS-Cu	117	0.34	8.3
OMS-Co	128	0.36	8.4
OMS-Ni	144	0.34	7.2
OMS-Zn	113	0.32	8.1

3.3. Raman spectroscopy

The Raman spectra obtained for the synthesized materials are presented in the Fig. 4. In general, all the solids show the same signals centered above 188, 291, 395, 486, 519, 588, 643 and 760 cm^{-1}. Because Mn atoms in the manganese dioxides are always 6-fold coordinated, the Raman bands of MnO_2 materials depend on the MnO_6 octahedral environments (e.g. edge/corner-sharing, interaction with water/cations in the tunnels or layers of MnO_2 materials) [18]. The observed Raman frequencies in the 500–700 and 200–500 cm^{-1} range have been assigned to the Mn–O stretching of MnO_6 octahedra and the Mn–O–Mn bending vibration in the MnO_2 octahedral lattice, respectively [19]. From Mn–O stretching range, the two sharp, high-frequency Raman bands at 588 and 643 cm^{-1} are indicative of a well developed tetragonal structure with an interstitial space consisting of (2×2) tunnels, and are assigned to the A_g mode [20]. An extensive work employing factor

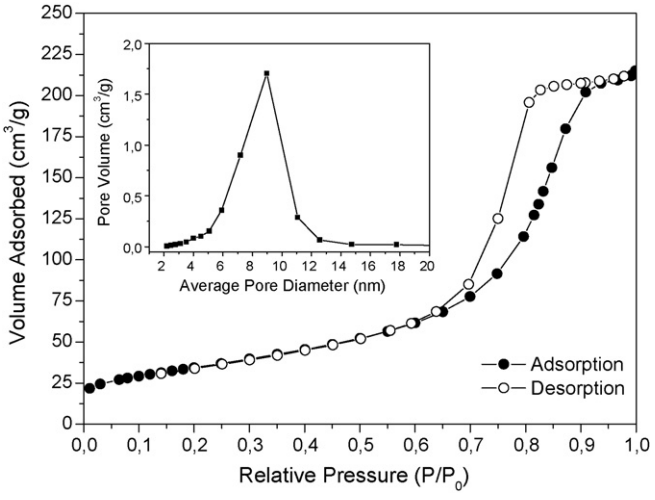

Fig. 3. Representative N_2 absorption/desorption isothermal plot of OMS solid. The insert shows the mesopore size distribution plot by BJH method.

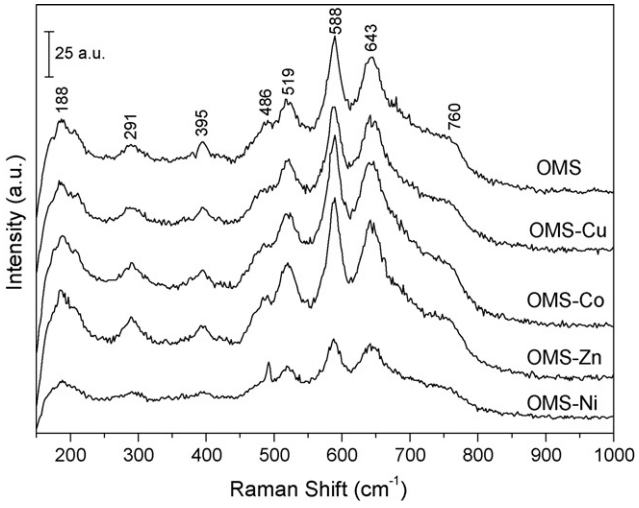

Fig. 4. Raman spectra of the synthesized materials.

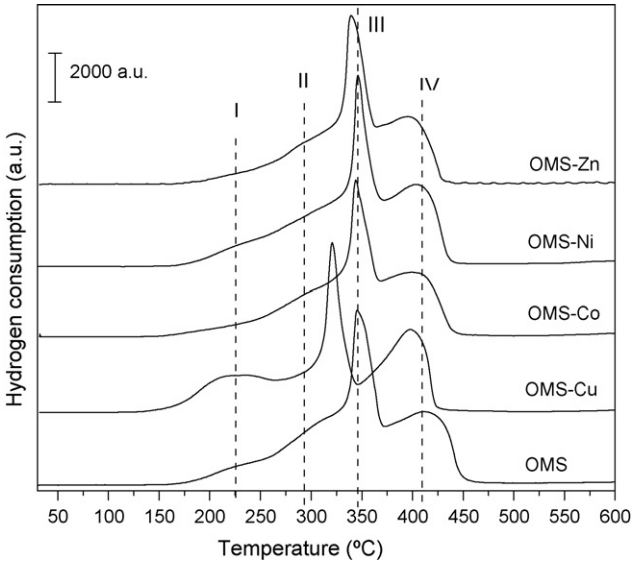

Fig. 5. Temperature programmed reduction (TPR) profiles for the synthesized materials.

group analysis has been developed by Gao et al. to assign the Raman bands in K-MnO_2 nanofibers [16]. Our data, Fig. 4, are in good agreement with both the number and the position of the bands reported by Gao et al. [16]. These authors reported that the presence of heavy tunnel cations damp the vibrational components perpendicular to the octahedral chains, the doping with different cations do not introduce any significative modification in the intensities of the vibrational modes and hence replacement of the K cations by the doping cations must be discarded.

Only signals corresponding to the K-MnO_2 structure are observed for all the synthesized materials. As for the XRD results the presence of any indication corresponding to the presence of the doping cation metal oxides is absent. However, all the observed vibrational modes appear at the same frequency whatever the presence or not of doping cations, although due to the heavier character of manganese with respect to oxygen the Mn–O vibrations must be supposed to mainly involve oxygen, the isomorphic substitution of manganese by other transition metal cations with different oxidation state will induce disorder in the lattice and may modify the nature and frequency of the active modes. Future work is necessary to establish the coordination of the doping cations in the synthesized materials.

3.4. Temperature programmed reduction (TPR-H_2)

The reduction of manganese oxides is often described by the successive reduction processes: $MnO_2 \rightarrow Mn_2O_3 \rightarrow Mn_3O_4 \rightarrow MnO$ [21]. However, the number and intensity of the peaks on the TPR curves can also depend on the different local environments of such species and the presence of other reducible ones. The TPR-H_2 profiles obtained for all synthesized materials are shown in Fig. 5. Four principal peaks were assumed from the TPR analysis. The assignation of each peak is as follows: Peak I, corresponding to the consumption of structural oxygen close to the surface, without decomposition of the material; Peak II, Peak III and Peak IV are related with the following reduction process: $MnO_2 \rightarrow Mn_2O_3$ (Peak II), $Mn_2O_3 \rightarrow Mn_3O_4$ (Peak III) and $Mn_3O_4 \rightarrow MnO$ (Peak IV) [21,22]. The apparent temperature of the TPR peaks for all synthesized materials is summarized in Table 3. For OMS, OMS-Co, OMS-Ni and OMS-Zn, the TPR profiles and the temperature values for the four peaks are very similar. On the other hand, for OMS-Cu solid, there is a significant decrease in the temperature of I, II and III reduction peaks and the presence of the TPR signal at lower temperature than 300 °C is more evident. These data suggest that the oxygen available for reduction is strongly influenced by the presence of Cu^{2+} in the synthesized material, strongly related to a higher oxygen mobility. Similar results have been described for cryptomelane-type manganese oxides modified with silver [23,24]. Studies in todorokite (OMS-1 with tunnel size about 6.9 Å) doped with Cu^{2+}, Ni^{2+}, Zn^{2+} and Mg^{2+} have established that the trends of change in reactivity and availability of the oxygen species due to the presence of the doping cations can be related to the changes in the heat of formation of the corresponding oxides and their electronegativity properties [25]. According to this, the presence of Cu in the material influences the reactivity of the oxygen atoms due to de formation of Mn–O–Cu bridges. This effect is evident in the OMS-Cu solid because copper has the higher electronegativity in the series of transition metal used (1.9 in front of 1.8 for Co and Ni, and 1.6 for Zn). Higher electronegativity of the doping cation promotes greater electronic delocalization and, consequently a weaker Mn–O bond [25]. The reduction temperature for the $Mn_3O_4 \rightarrow MnO$ (Peak IV) process hardly on modifying the doping cation, suggesting an important role of the structural and morphological properties of the material in the reactivity of lattice oxygen. This, considering the different crystalline structures obtained during the reduction of MnO_2 to MnO.

The enhanced oxygen lability in OMS-Cu solid may be related to the formation of anion vacancies, which would improve the reactivity of this materials in oxidation process, as has been established in mixed oxides like as $Ce_{1-x}M_xO_{2-y}$ systems [26,27]. In fact, for CuO/CeO_2 mixed oxides (one of the most studied catalysts for the CO-PROX reaction) [28–31], it has been reported by TPR analysis that the presence of highly dispersed CuO on the CeO_2 surface and/or the partial replacement of Ce^{4+} by Cu^{2+} in the CeO_2 fluorite structure improved the redox properties of ceria [32,33]. This better reducibility influences the catalytic activity of the materials,

Table 3
Temperature-reduction peaks for the synthesized materials.

Code	Temperature peak (°C)			
	Peak I	Peak II	Peak III	Peak IV
OMS	234	306	350	410
OMS-Cu	207	247	321	394
OMS-Co	232	302	347	401
OMS-Ni	239	308	348	400
OMS-Zn	250	304	343	393

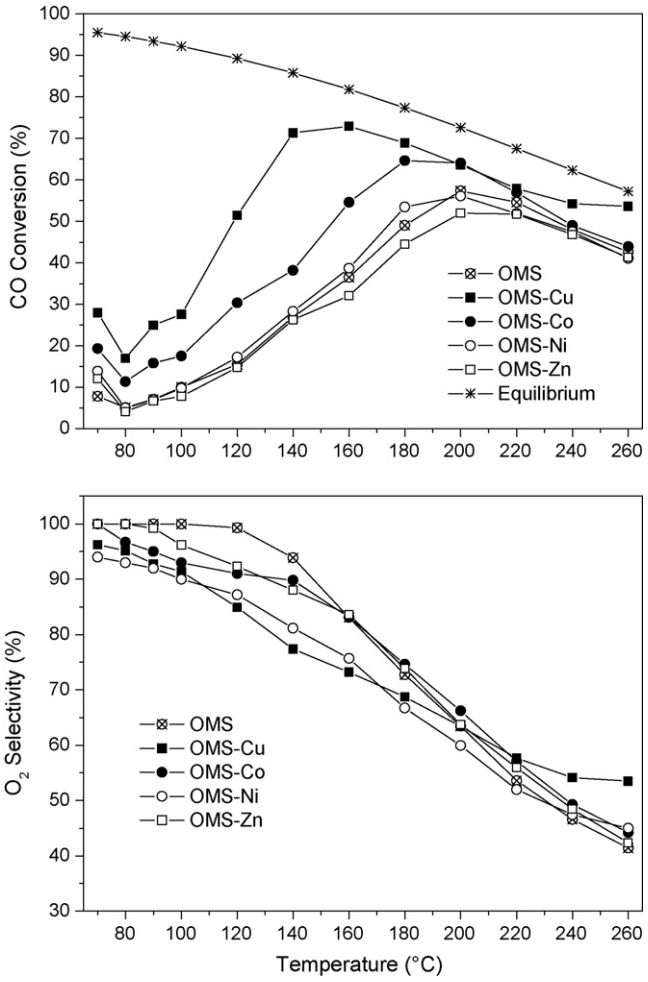

Fig. 6. Variation of CO conversion and O_2 selectivity with the reaction temperature for the preferential oxidation of CO in presence of hydrogen, over the powder synthesized materials.

in such a way that the most active catalysts are the most reducible ones.

3.5. Catalytic activity: preferential oxidation of CO in presence of H_2 (PROX)

The catalytic activity of the synthesized materials for CO oxidation and their selectivity to CO_2 as a function of reaction temperature is shown in Fig. 6. All prepared solids were active in the PROX reaction and present a similar CO conversion at temperatures higher than 180 °C, closer to those determined by the equilibrium. However, OMS-Cu and OMS-Co solids present higher activity at low temperatures than the unmodified cryptomelane. Thus, it is evident the beneficial effect of the presence of the doping transition metals in the material, in order to improve their catalytic properties. The O_2 selectivity is very similar in all the materials and decreases on increasing the temperature. These results suggest that the activation energy of the H_2 oxidation is higher than that of the CO oxidation, maintaining selectivity higher than 80% at reaction temperatures lower than 140 °C. Taking into account that, at equal temperatures, the CO conversion obtained for each catalyst is different, the competition between CO and H_2 for the same O_2 molecule occurs with different reactive partial pressures. Thus, in order to evaluate the catalytic performances of the solids in equivalent conditions, the relationship between the CO conversion and the O_2 selectivity was depicted in Fig. 7. All catalysts present an O_2

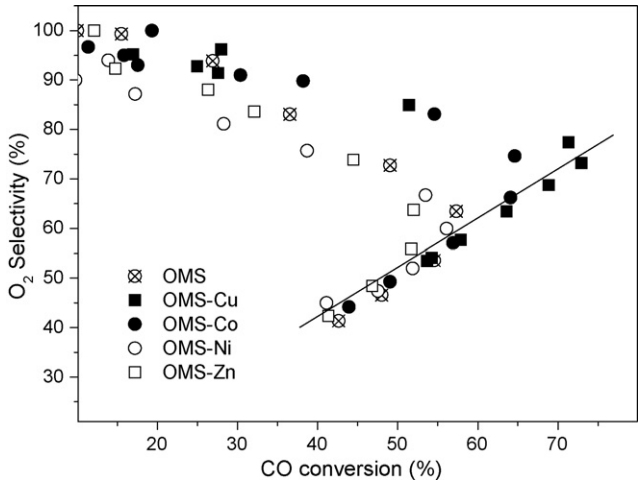

Fig. 7. O_2 selectivity vs. CO conversion as criteria to evaluate the efficiency of the studied catalysts.

selectivity higher than 85% at CO conversions below 20%, being the thermodynamics the leading factor for the CO and H_2 oxidation, as can be expected from the enthalpy values of the respective oxidation reactions (Eqs. (4) and (5)). However, at CO conversions above 20%, a different behavior is observed. For temperatures lower than 180 °C, where the CO conversion is far for the equilibrium limitations (Fig. 6), the O_2 selectivity obtained at the same CO conversion for each catalyst, decreasing faster for OMS, OMS-Ni and OMS-Zn solids, in comparison with OMS-Cu and OMS-Co ones. For temperatures higher than 180 °C (Fig. 6), after reaching its maximum CO conversion, all catalyst follows the same tendency, where the O_2 selectivity does not change for the same CO conversion, independently of the solid. This trend is represented with a straight line in Fig. 7, and can be correlated with the limitation imposed by the equilibrium situation, under the reactions conditions employed in this work. Because the OMS-Cu solid reach higher CO conversions than that of OMS-Co one, keeping the same O_2 selectivity, the first one can be considered as the more efficient catalyst in the evaluated series.

In general, the presence of Cu in catalysts for CO oxidation results in enhanced catalytic properties, promoting the redox properties of the material, as in Hopcalite catalysts [34], or facilitating the CO chemisorption process during the reaction [35]. For structures like OMS-2-type doped with M = Cu^{2+}, Co^{2+} or Ag^{+}, Xia et al. [36] have established that charge transfer along the M–O–Mn bond may be responsible for CO oxidation. In this mechanism, the reversible electron transfer along the M–O–Mn bridge suppose the reduction and reoxidation of the doping cation together with the Mn^{4+} of the oxide structure, in a complete redox cycle where chemisorbed O_2 is also involved. On the other hand, it is widely accepted that CO oxidation over manganese oxides proceeds via Mars-van-Krevelen mechanism which involves the reaction of adsorbed CO with the labile oxygen lattice [37]. The reactivity is associated with the capacity of manganese to form various oxidation states, e.g., redox pairs Mn^{2+}/Mn^{3+} or Mn^{3+}/Mn^{4+}, and "oxygen available" in the oxide lattice. With respect to this, as was established by TPR analysis, the presence of Cu in the cryptomelane catalyst greatly improves the mobility and availability of oxygen near the oxide surface, associated to the influence of Cu in the Mn–O bond strength. Similar results have been founded by Gac et al. for cryptomelane-type manganese oxides doped with Ag^{+} [23,24]. In these materials, a high reactivity toward CO oxidation at low temperatures has been attributed to the structural changes and increased oxygen mobility induced by the presence of silver. Therefore, according to this mechanism, over OMS-Cu solid, the carbon monoxide molecule

reacts with the labile oxygen species, induced by the presence of Cu in the structure, and the resulting oxygen vacancies are removed by adsorption of oxygen molecules from the gas phase.

4. Conclusions

Using the milling method, it is possible to synthesize cryptomelane-type manganese dioxide nanomaterials modified with various transition metals cations (Cu, Co, Ni and Zn) without significant changes in their structural and textural characteristics. Modified cryptomelane solids present high catalytic activity in the preferential oxidation of CO reaction, being more active the cryptomelane modified with Cu. This tendency is correlated with the reducibility of this material, together with the oxygen lability promoted by the doping cation.

Acknowledgments

The financial support by Junta de Andalucia (TEP106) and Spanish MYCT (MAT2006-12386-C05-01) are gratefully acknowledged. F. Romero-Sarria thanks the Spanish Ministerio de Educación y Ciencia for her contract (Ramon y Cajal Programme). W.Y. Hernández thanks the AlBan program of the European Union for the fellowship awarded (E06D101739CO).

References

[1] T.V. Choudhary, D.W. Goodman, Catal. Today 77 (2002) 65.
[2] E.D. Park, D. Lee, H.C. Lee, Catal. Today 139 (2009) 280.
[3] B. Solsona, G.J. Hutchigns, T. García, S.H. Taylor, New. J. Chem. 28 (2004) 708.
[4] C. Jones, K.J. Cole, S.H. Taylor, M.J. Crudace, G.J. Hutchings, J. Mol. Catal. A 305 (2009) 121.
[5] Z.R. Tian, W. Tong, J.Y. Wang, N.G. Duan, V.V. Krishnan, S.L. Suib, Science 276 (1997) 926.
[6] D.M. Frías, S. Nousir, I. Barrio, M. Montes, L.M. Martínez, M.A. Centeno, J.A. Odriozola, Appl. Catal. A 325 (2007) 205.
[7] M.I. Dominguez, P. Navarro, F. Romero-Sarria, D. Frías, S.A. Cruz, J.J. Delgado, M.A. Centeno, M. Montes, J.A. Odriozola, J. Nanosci. Nanotechnol. 9 (2009) 3837.
[8] L.C. Wang, L. He, Y.M. Liu, Y. Cao, H.Y. He, K.N. Fan, J.H. Zhuang, J. Catal. 264 (2009) 145.
[9] F.G. Durán, B.P. Barbero, L.E. Cadús, C. Rojas, M.A. Centeno, J.A. Odriozola, Appl. Catal. B 92 (2009) 194.
[10] R.N. DeGuzman, Y.F. Shen, E.J. Neth, S.L. Suib, C.L. O'Young, S. Levine, J.M. Newman, Chem. Mater. 6 (1994) 815.
[11] S.L. Brock, N. Duan, Z.R. Tian, O. Giraldo, H. Zhou, S.L. Suib, Chem. Mater. 10 (1998) 2619.
[12] I. Barrio, I. Legórburu, M. Montes, M.I. Domínguez, M.A. Centeno, J.A. Odriozola, Catal. Lett. 101 (2005) 151.
[13] D. Frías, S. Nousir, I. Barrio, M. Montes, T. López, M.A. Centeno, J.A. Odriozola, Mater. Charact. 58 (2007) 776.
[14] Y.G. Yin, W.Q. Xu, S.L. Suib, Inorg. Chem. 34 (1995) 4187.
[15] Y. Ding, X. Shen, S. Sithambaram, S. Gomez, R. Kumar, V. Mark, V. Crisostomo, S.L. Suib, M. Aindow, Chem. Mater. 17 (2005) 5382.
[16] T. Gao, M. Glerup, F. Krumeich, R. Nesper, H. Fjellvag, P. Norby, J. Phys. Chem. C 112 (2008) 13134.
[17] K.S.W. Sing, D.H. Everett, R.A.W. Haul, L. Moscou, R.A. Pierotti, J. Rouquérol, T. Siemieniewska, Pure Appl. Chem. 57 (1985) 603.
[18] H.S. Kim, P. Stair, J. Phys. Chem. B 108 (2004) 17019.
[19] C.M. Julien, M. Massot, C. Poinsignon, Spectrochim. Acta, Part A 60 (2004) 689.
[20] M. Polverejan, J.C. Villegas, S.L. Suib, J. Am. Chem. Soc. 126 (2004) 7774.
[21] M. Tsuji, S. Komarneni, J. Mater. Res. 8 (1993) 611.
[22] L. Christel, A. Pierre, A.M. Rousset Abel, Thermochim. Acta 306 (1997) 51.
[23] W. Gac, G. Giecko, S. Pasieczna-Patkowska, T. Borowiecki, L. Kepinski, Catal. Today 137 (2008) 397.
[24] W. Gac, Appl. Catal. B 75 (2007) 107.
[25] Y.G. Yin, W.Q. Xu, Y.F. Shen, S.L. Suib, Chem. Mater. 6 (1994) 1803.
[26] W.Y. Hernández, M.A. Centeno, F. Romero-Sarria, J.A. Odriozola, J. Phys. Chem. C 113 (2009) 5329.
[27] H. Bao, X. Chen, J. Fang, Z. Jiang, W. Huang, Catal. Lett. 125 (2008) 160.
[28] G. Avgouropoulos, T. Ioannides, H.K. Matralis, J. Batista, S. Hocevar, Catal. Lett. 73 (2001) 33.
[29] I. López, T. Valdés-Solís, G. Marbán, Int. J. Hydrogen Energy 33 (2008) 197.
[30] N. Bion, F. Epron, M. Moreno, F. Mariño, D. Duprez, Top. Catal. 51 (2008) 76.
[31] E.D. Park, D. Lee, H.Ch. Lee, Catal. Today 139 (2009) 280.
[32] J. Xiaoyuan, L. Guanglie, Z. Renxian, M. Jianxian, Ch. Yu, Z. Xiaoming, Appl. Surf. Sci. 173 (2001) 208.
[33] A. Martínez-Arias, D. Gamarra, M. Fernández-García, A. Hornés, P. Bera, Zs. Koppány, Z. Schay, Catal. Today 143 (2009) 211.
[34] S.B. Kanungo, J. Catal. 58 (1979) 419.
[35] Z.Y. Pu, X.S. Liu, A.P. Jia, Y.L. Xie, J.Q. Lu, M.F. Luo, J. Phys. Chem. C 112 (2008) 15045.
[36] G.G. Xia, Y.G. Yin, W.S. Willis, J.Y. Wang, S.L. Suib, J. Catal. 185 (1999) 91.
[37] K. Ramesh, L. Chen, F. Chen, Y. Liu, Z. Wang, Y.F. Han, Catal. Today 131 (2008) 477.